Secondary radiation in transmission-type X-ray tubes: simulation, practical issues and solution in the context of X-ray microtomography

Matthieu N. Boone[a], Jelle Vlassenbroeck[b], Steven Peetermans[c], Denis Van Loo[a,d], Manuel Dierick[a], Luc Van Hoorebeke[a]

[a] *Ghent University, Dept. Physics and Astronomy*
Proeftuinstraat 86; B-9000 Gent, Belgium
[b] *inCT*
Technologiepark 3; B-9052 Zwijnaarde, Belgium
[c] *Neutron Imaging and Activation Group*
Paul Scherrer Institut; Villigen, Switzerland
[d] *Ghent University, Dept. Soil Management and Soil Care*
Coupure Links 653; B-9000 Gent, Belgium

Abstract

In laboratory-based X-ray radiography and computed tomography, the X-rays are assumed to originate from one single focal spot with a finite spot size, which is generated by focussing accelerated electrons on the target material. However, apart from this focal spot, X-rays can also be produced elsewhere in the tube system. A major contribution of this parasitic radiation originates from electrons that are backscattered from the target material, into the X-ray tube system, where they can produce so-called *off-focus* or *secondary* X-rays. This phenomenon has been widely studied for rotating anode X-ray tubes in medical imaging systems, but not for transmission-type microfocus X-ray tubes. This paper presents a study on the origin of secondary radiation in this kind of X-ray tubes, which is performed by Monte Carlo simulations and by experimental measurements. The impact of this phenomenon on the imaging process is studied, and two correction methods are proposed, both on the hardware and on the software level.

Keywords: X-ray tube, focal spot, Monte Carlo simulation, secondary radiation, off-focal radiation, BEAMnrc
PACS: 87.59.B-, 07.85.Fv

1. Introduction

In laboratory-based X-ray radiography and tomography, X-rays are usually produced by an X-ray tube. In such a system, electrons emitted from the cathode are accelerated and focussed on the target, which consists of a high-Z material where Z is the atomic number, usually tungsten or molybdenum. The electrons are decelerated in this target material, producing bremsstrahlung and characteristic X-rays. However, some electrons are backscattered into the X-ray tube system. In high-power rotating anode X-ray tubes, these electrons are accelerated back towards the anode under the influence of the electric field, interacting again with the target material and thus generating additional radiation, usually originating outside the primary focal spot. This effect has previously been called secondary, parasitic, extrafocal or off-focal radiation and can often be recognised by the presence of some sort of secondary image in the radiographs. Although it has often been ignored in spectrum calculations[1], it has been shown that the contribution of the effect cannot be neglected[2].
In contrast to high-power rotating anode X-ray tubes, transmission-type microfocus X-ray tubes usually consist of a separate acceleration module and focussing module. Due to this modular design, the electric field and the electron acceleration near the target is negligible. The backscattered electrons are not accelerated towards the target, but instead they interact with the tube housing material, creating additional X-rays inside this structure. Depending on the tube design and used materials, the origin, shape and spectrum of this secondary radiation can vary. Although several studies have been published on the topic of the secondary radiation in rotating anode X-ray tubes[2, 3, 4, 5, 6] including several patents for reduction (e.g. patent #6052434, patent #4905268 and patent #5493599), the effect is almost undocumented for transmission-type microfocus tubes[7].
This paper presents a study of the secondary radiation effect in a transmission-type microfocus X-ray tube, which has been observed at the the high-resolution micro-CT (μCT) setup of the Ghent University Center for X-ray Tomography (UGCT – `http://www.ugct.ugent.be`)[8]. This effect became evident in μCT scans where unrealistic density profiles appeared. The total X-ray source was simulated using BEAMnrc[9, 10, 11], which is based on the EGSnrc[12] code system, and secondary radiation was shown to be caused by the internal design of the tube. Both a hardware and a software correction for this effect are presented, along with their results.

2. Materials and methods

2.1. Experimental setup

All experiments were carried out using a FeinFocus X-ray tube with the FXE160.51 transmission head. The target is a 5 μm thick tungsten layer on a diamond backing (thickness 250 μm). Tube voltage was set to 80 kV at a tube current of 62.5 μA. This resulted in a primary spot size of approximately 3 μm.

Table 1: Experimental parameters for both radiographs and CT scan

	radiograph	CT scan
source-to-object distance [mm]	68.8	20.3
source-to-detector distance [mm]	1395	1395
detector pixel pitch [μm]	200	400
detector resolution	2048×2048	1024×1024
radiograph voxel size [μm]	9.86	5.83
hardware filter	–	1 mm Al
# projection images	–	1201
radiograph exposure time [ms]	4000	2000

Images were acquired using a PerkinElmer XRD 1620 CN3 CS flat-panel detector (pixel size: $200\times200\,\mu m^2$) with CsI scintillator. The secondary radiation effect was studied using both radiography and tomography (CT) data. The sample used for radiography was a graphite cylinder (diameter 0.9 mm) with a small lead drop. This small drop acts approximately as an "'impulse function"', to visualise the source distribution. A μCT scan of a sandstone (diameter 4.8 mm) was used to illustrate the effect of the corrections on CT reconstruction. The experimental parameters of both radiography and CT scan are given in Table 1. The software package Octopus[13] was used for the tomographic reconstruction. A simple beam-hardening correction was applied on the data[13].

2.2. Monte Carlo simulations

Simulations of the X-ray tube were carried out using BEAMnrc. It has been shown that the EGSnrc/BEAMnrc system performs well in the calculation of charged particle backscattering for the energy range of interest[14, 15]. Detailed design plans of the X-ray tube were provided by the manufacturer of the system (Figure 1). The electrons originate from the left-hand side of the figure, following the dotted central line, passing the aperture in the middle of the figure. The electrons hit the target at the right-hand side of the figure, creating X-rays. Some of these electrons are backscattered into the tube system. Due to the large aspect ratio of the aperture (a length of 2.77 mm at a diameter of 0.7 mm), the fraction of backscattered electrons passing this aperture can be neglected. For this reason, simulations were limited to the final 1 cm of the tube head, neglecting the radiation originating from behind the aperture. The electron beam was simulated as a pencil beam with a finite diameter of 3 μm, exactly on the symmetry axis. Several acceleration voltages (40 kV, 80 kV and 120 kV) were simulated. For each simulation 10 runs of 5000000 electrons were used, each with a different random number seed to minimize accidental correlations. Uniform bremsstrahlung splitting (splitting factor 1000) was applied for variance reduction[9]. Cutoff energies were set to 0. Electron impact ionization (Kawrakow) and atomic relaxations were turned on to obtain characteristic radiation. Photon cross-sections were imported from the NIST

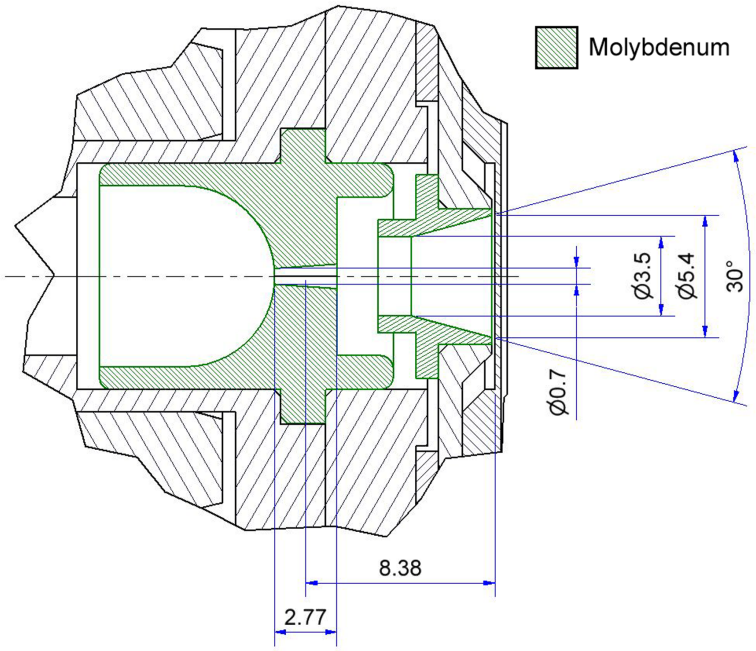

Figure 1: Schematic drawing of the X-ray tube head. The tungsten target is at the right-hand side of the drawing. Structures made in molybdenum are indicated. All distances are given in millimeter.

XCOM library. The simulated geometry can be seen in Figure 2, where the pencil beam follows the z-axis from $z = 0.000\,\text{cm}$ to $z = 1.000\,\text{cm}$, where the target material begins. Only X-rays registered at the scoring plane $z = 5.000\,\text{cm}$ and $-0.500\,\text{cm} \leq x, y \leq 0.500\,\text{cm}$ are tallied, corresponding to a cone angle of 11.3°, which is a realistic value for CT. The attenuation in air between target and detector is not included by assuming vacuum conditions inside and outside the tube. For each tallied X-ray, the x, y and z position of the creation of this X-ray as well as its energy is logged. For the analysis of the X-ray spectrum, simulations at an acceleration voltage of 80 kV were performed for both the complete tube system and the system with the molybdenum structures replaced by vacuum. All other simulation parameters were kept unchanged.

2.3. Correction methods

A software correction was implemented in LabView® 8.6 to reduce the secondary radiation artifacts. It is derived from the assumption that the measured image I_{meas} is composed of two separate contributions: one projection image I_{FS} created by the primary focal spot, and one projection image I_{SS} created

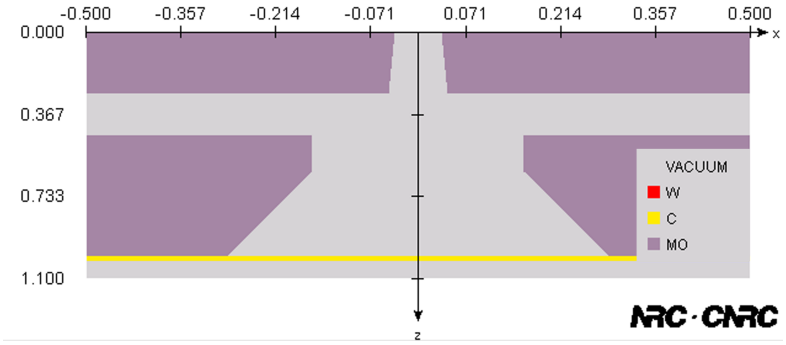

Figure 2: Simulated geometry of the FeinFocus design. The z-axis is also the symmetry axis. Electrons originate from $|x, y| \leq 0.0003\,\text{cm}$, $z = 0.0000\,\text{cm}$. The thin tungsten target is not visible on the diamond backing. All distances are indicated in centimeter.

by the secondary source:

$$I_{meas} = I_{FS} + I_{SS} \tag{1}$$

in which both I_{FS} and I_{SS} are a convolution of the ideal image I_{ideal} and the distribution of each source. The primary spot S_{prim} has a very narrow distribution around $|x, y| = 0\,\text{cm}$, while the secondary source has a distribution S_{sec} which comprises all photons not included in S_{prim}:

$$I_{meas} = I_{ideal} * S_{prim} + I_{ideal} * S_{sec} \tag{2}$$

The distribution S_{prim} is assumed to be very narrow and is approximated by an ideal Dirac δ function. When the measured intensity is convolved with a function S'_{sec} approximating the secondary source S_{sec} and second-order contributions are neglected, the contribution of the secondary source can be approximated:

$$\begin{aligned} I_{meas} * S'_{sec} &= I_{ideal} * (S_{prim} * S'_{sec}) + I_{ideal} * (S_{sec} * S'_{sec}) \\ &\approx I_{ideal} * S'_{sec} + I_{ideal} * (S_{sec} * S'_{sec}) \qquad (3) \\ &\approx I_{ideal} * S'_{sec} \qquad (4) \\ &\approx I_{SS} \end{aligned}$$

This contribution is then substracted from the measured image, resulting in an approximation of the image made by the primary focal spot.

The hardware correction consists of a thin lead collimator with a diameter of approximately 1 mm that can be mounted on the X-ray tube. Special care must be taken to position the opening of the collimator well aligned relative to the electron beam axis, and close enough to the X-ray tube. However, as it hinders the heat transfer from the target material and target backing, it should remain

at a certain distance. A typical working distance of approximately 2 mm was used.

3. Results

3.1. Simulation

Taking advantage of the cylindrical symmetry of the setup, the radial distribution of the origin of the tallied X-rays is plotted in Figure 3. The intensity axis depicts the number of tallied photons and has been clipped for scaling reasons. Figure 4 shows the cumulative normalised intensity as a function of the distance r from the symmetry axis. Depending on the tube voltage, approximately 85% to 90% of the radiation originates from the primary focal spot ($r \approx 0$ in Figure 4). It can be clearly seen that most of the secondary radiation for this specific geometry originates from a ring (inner radius ≈ 0.16 cm and outer radius ≈ 0.28 cm) around the primary focal spot, which can be associated with the oblique structure closest to the target. The peak at $r = 0.16$ cm can be associated with the edge of this structure perpendicular to the target plane. This can also be verified in the 2D distribution of the generated X-rays, as a function of both the z position and the distance r from the symmetry axis (Figure 5), where $z = 1.000$ corresponds to the W target. The geometry depicted in Figure 2 can be easily recognized in this distribution. It must be noted here that a part of the off-focal radiation originates from the target material itself. This radiation can originate from electrons that are backscattered twice, and fluorescent radiation from the target after absorption of X-rays created mainly in the tube system.
The energy spectrum of radiation with and without the molybdenum structures is shown in Figure 6(a). The difference between both spectra, i.e. the contribution of the secondary radiation, is shown together with the total spectrum in Figure 6(b). The difference between primary and secondary spectrum can be mostly found in the characteristic radiation of tungsten and molybdenum, while the bremsstrahlung spectrum remains similar. Additionally, some characteristic radiation from tungsten is present in the secondary radiation, originating from the target plane as discussed earlier.

3.2. Correction methods

Both correction methods have been applied to the radiograph of the lead dot. It can be seen in Figure 7(a) that the total X-ray source (primary focal spot and secondary radiation source) is imaged, and the contribution of the secondary radiation is clearly recognised as a ring-shaped structure. The results of the software correction can be seen in Figure 7(b). The estimated secondary source S'_{sec} is a ring structure of which the geometric parameters are derived directly from the simulation (outer radius: 2.75 mm; inner radius: 1.7 mm) and the magnification geometry. The magnitude of the contribution is obtained by trial and error. The result of the hardware correction can be seen in Figure 7(c). It is clear that the secondary radiation effect is removed almost completely.

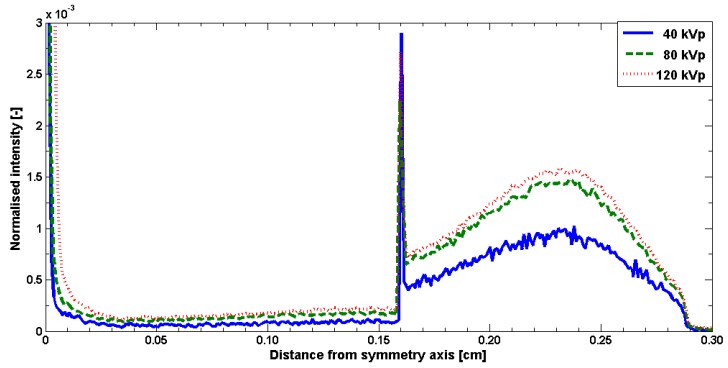

Figure 3: Radial intensity distribution of the origin of the X-rays tallied at the scoring plane for different tube voltages.

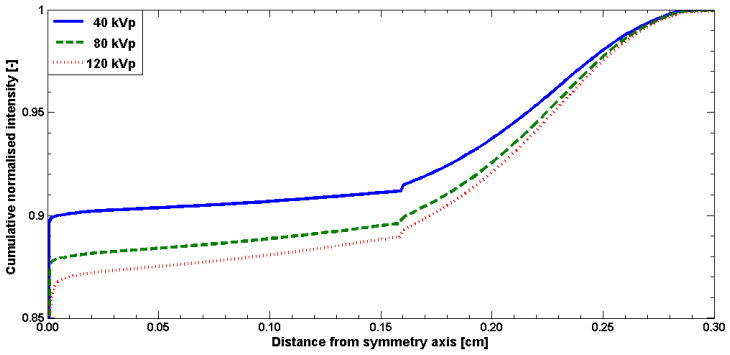

Figure 4: Cumulative radial intensity distribution of the origin of the X-rays tallied at the scoring plane for different tube voltages.

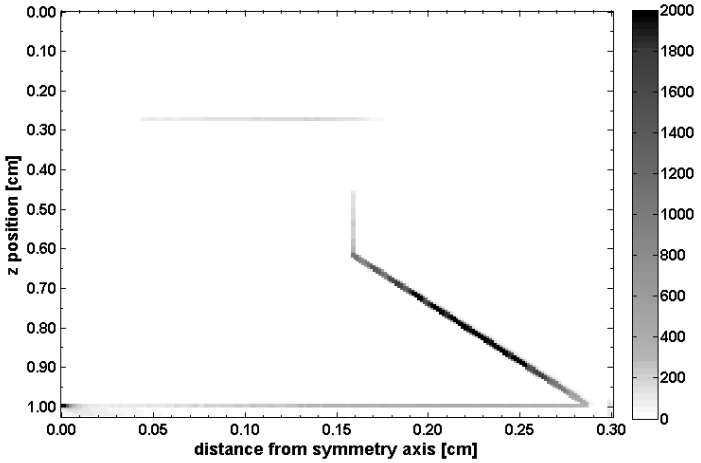

Figure 5: Distribution of the origin of the X-rays at a tube voltage of 80 kVp as a function of the z position in the simulation and the distance from the symmetry axis. The gray scale has been clipped to improve visibility.

The effect of the secondary radiation on a reconstructed CT slice can be seen in false color in Figure 8(a). The overlap of the primary attenuation image with the secondary attenuation image results in an increased reconstructed attenuation coefficient at the bulk of the sample, giving rise to an inverted cupping effect in the CT slice. Although this effect is very small and hard to visualize, it can still hinder good image analysis. The software correction, again using theoretically derived parameters except for the magnitude of the contribution, removes almost completely this artifact (Figure 8(b)). A similar result is obtained with the hardware correction (Figure 8(c)). It must be noted that the scaling in the reconstructed slices varies slightly, caused by the magnitude of the secondary radiation effect.

4. Discussion

The simulation of the secondary radiation effect yields results that correspond well with the experimental observation. The effect can be easily associated with design features inside the tube head. Nevertheless, the secondary radiation effect in general can not be removed by alteration of the design. This can be verified by the simulation of an alternative design of the tube system, where the inclined structure close to the target material is not present. A simple design, consisting of a slab with only an aperture is shown in Figure 9. The simulation of this design (Figure 10) shows a similar ring-shaped profile, with a high intensity at the edge of the aperture (perpendicular to the target material) and a low intensity on the face of the aperture (parallel to the target). The

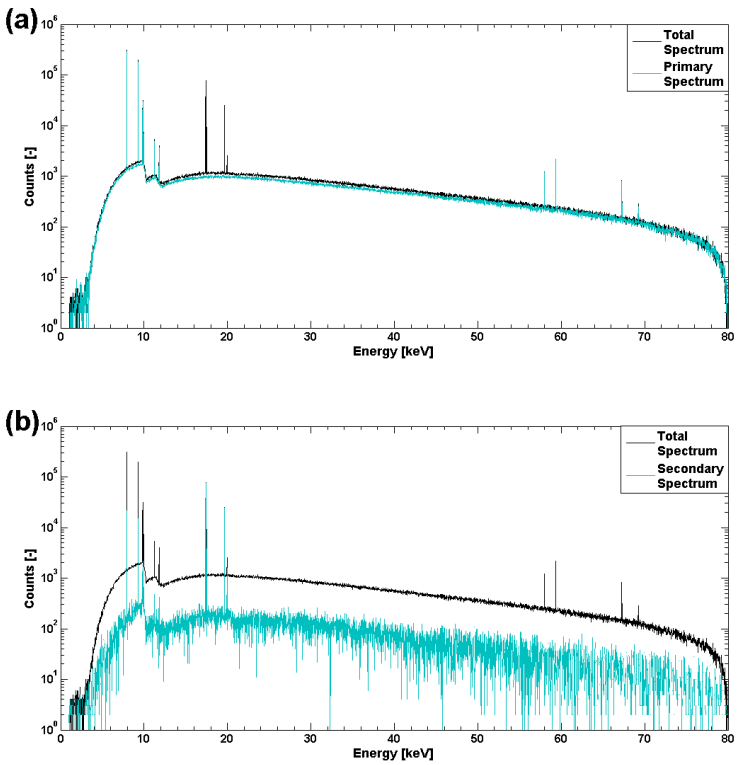

Figure 6: (a) The X-ray spectrum of the tube system and the tube system without molybdenum structures, corresponding to the spectrum of the primary focal spot. (b) The X-ray spectrum of the tube system and the difference between the total spectrum and the primary spectrum, corresponding to the spectrum of the secondary radiation.

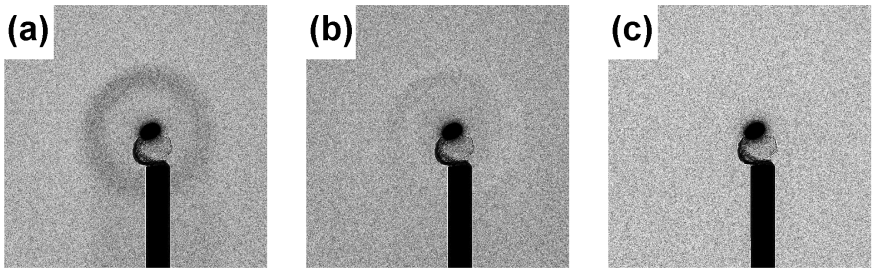

Figure 7: Radiograph of a small lead drop. (a) Radiograph without collimator (b) Post-processed radiograph (c) Radiograph with collimator

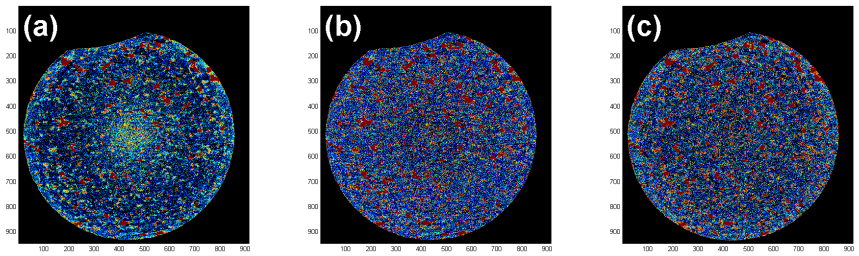

Figure 8: Reconstructed CT slice of a sandstone in false color. (a) Data acquired without collimator (b) use of post-processed projection data (c) Data acquired with collimator

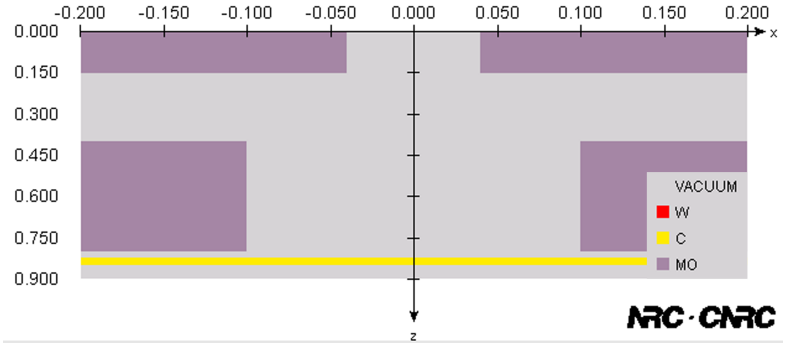

Figure 9: Simulated geometry of the alternative design with distance d between aperture and target $d = 0.25\,\text{mm}$. The z-axis is also the symmetry axis. Electrons originate from $\|x, y| \leq 0.0003\,\text{cm}$, $z = 0.0000\,\text{cm}$. The thin tungsten target is not visible on the diamond backing. All distances are indicated in centimeter.

intensity of the latter is highly dependant on the distance between the target material and the aperture. This distance should ideally be zero, but as contact between both structures should be avoided this is practically not possible. It must also be noted that a large aperture can be benificial in order to allow the usage of a collimator with a large diameter, which is more practical.

Although software correction of the secondary radiation yields a well-corrected image and CT reconstruction, it fails to remove the effect completely (Figure 7(b)). This can be due to several reasons. As the secondary radiation is not originating from the target, the distance from X-ray source to sample and detector is slightly different for this radiation. As a consequence, the geometric magnification of the effect is not exactly determined. Additionally, the shape of the secondary focal spot is approximated by a uniform ring-structure. It can be seen in Figure 3 that this uniformity is not consistent with the simulations. Another reason can be found in equation (4), where $|S_{sec} * S'_{sec}|$ is neglected. Simulations have shown this contribution S_{sec} to be of the order of 10% (Figure 4), which makes this assumption questionable.

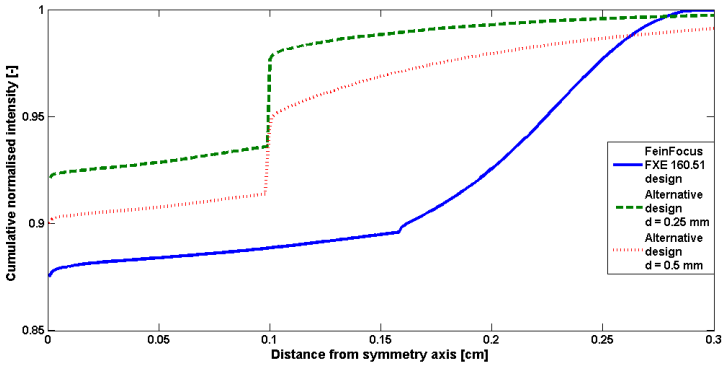

Figure 10: Normalised cumulative counts for the geometry shown in Figure 9 with distance d between aperture and target $d = 0.5\,\text{mm}$ and $d = 0.25\,\text{mm}$, and the FXE160.51 design as discussed in previous sections

As mentioned before, the intensity of S'_{sec} varies depending on the experimental conditions and is to be set by trial and error based on the projection data. This induces operator-dependant results. A realistic a-priori estimation of this intensity is not possible, due to the non-uniformity of the secondary radiation and the spectrum of the created X-rays. In this case, a tungsten target is used, while the inner structure of the tube is made of molybdenum. Furthermore, the X-rays originating from the inner structure are attenuated by the target material. Both effects will often result in a different average X-ray energy from the inner structure and thusa different relative contribution of the secondary radiation.

A third limitation of the software correction is the presence of highly attenuating structures outside the field of view. Due to the very large size of the secondary source compared to the primary spot, these structures can have secondary projections inside the field of view. However, as their primary projection is not imaged, they can not be corrected. This effect is commonly caused by sample holders, creating a vertical change of the reconstructed attenuation coefficient inside the sample.

5. Conclusion

In this work, we have shown that secondary or off-focal radiation arises from electron back-scattering in transmission-type microfocus X-ray tubes. This effect can be successfully simulated using Monte Carlo simulations, from which the shape and the intensity of this secondary source can be derived. For the experimental setup at UGCT, this effect has a non-negligible contribution of approximately 10% to the X-ray flux at the detector plane. Consequently, artifacts can be seen on X-ray radiographs and tomographic reconstructions. To

minimize these artifacts, two separate correction methods have been proposed. A post-processing software filter can be applied to estimate and correct for the contribution of the secondary source in the measured image. Although this works well in some cases, it has several limitations such as the limited field of view of the detector plane. A hardware solution, consisting of a simple collimator, can also be used to minimize these artifacts.

6. Acknowledgements

The authors are very grateful to Thorsten Froeba from X-RAY WorX GmbH for the detailed description of the X-ray tube and the fruitful discussions on this topic. The Fund for Scientific Research Flanders(FWO-Vlaanderen)is greatfully acknowledged for their financial support(project G.0100.08).

References

[1] G. G. Poludniowski, Calculation of x-ray spectra emerging from an x-ray tube. Part II. X-ray production and filtration in x-ray targets, Med. Phys. 34 (6) (2007) 2175–2186.

[2] R. Birch, The spectrum and intensity of extra-focal (off-focus) radiation, Br. J. Radiol. 49 (1976) 951–955.

[3] R. H. Miettunen, Measurement of extrafocal radiation by computed radiography, Br. J. Radiol. 65 (1992) 238–241.

[4] J. Hsieh, Computed tomography : principles, design, artifacts, and recent advances, SPIE Optical Engineering Press, 2003.

[5] Z. Wen, N. K. Pelc, W. R. Nelson, R. Fahrig, Study of increased radiation when an x-ray tube is placed in a strong magnetic field, Med. Phys. 34 (2) (2007) 408–418.

[6] E. S. M. Ali, D. W. O. Rogers, Quantifying the effect of off-focal radiation on the output of kilovoltage x-ray systems, Med. Phys. 35 (9) (2008) 4149–4160.

[7] J. Vlassenbroeck, Advances in laboratory-based X-ray microtomography, Ph.D. thesis, Ghent University, 2009.

[8] B. Masschaele, V. Cnudde, M. Dierick, P. Jacobs, L. Van Hoorebeke, J. Vlassenbroeck, UGCT: New x-ray radiography and tomography facility, Nucl. Instrum. Meth. Phys. Res. A 580 (1) (2007) 266–269.

[9] D. W. O. Rogers, B. A. Faddegon, G. X. Ding, C. M. MA, J. WE, T. R. Mackie, BEAM - A Monte-Carlo code to simulate radiotherapy treatment units, Med. Phys. 22 (5) (1995) 503–524.

[10] E. Mainegra-Hing, I. Kawrakow, Efficient x-ray tube simulations, Med. Phys. 33 (8) (2006) 2683–2690.

[11] M. Fragoso, I. Kawrakow, B. A. Faddegon, T. D. Solberg, I. J. Chetty, Fast, accurate photon beam accelerator modeling using BEAMnrc: a systematic investigation of efficiency enhancing methods and cross-section data, Med. Phys. 36 (12) (2009) 5451–5466.

[12] I. Kawrakow, Accurate condensed history Monte Carlo simulation of electron transport. I. EGSnrc, the new EGS4 version, Med. Phys. 27 (3) (2000) 485–498.

[13] J. Vlassenbroeck, M. Dierick, B. Masschaele, V. Cnudde, L. Van Hoorebeke, P. Jacobs, Software tools for quantification of X-ray microtomography, Nucl. Instrum. Meth. Phys. Res. A 580 (1) (2007) 442–445.

[14] E. S. M. Ali, D. Rogers, Benchmarking EGSnrc in the kilovoltage energy range against experimental measurements of charged particle backscatter coefficients, Phys. Med. Biol. 53 (2008) 1527–1543.

[15] E. S. M. Ali, D. Rogers, Energy spectra and angular distributions of charged particles backscattered from solid targets, J. Phys. D: Appl. Phys. 41 (2008) 055505 (9pp).